Highly Miniaturized Multiband Bandpass Filter Design Based on a Stacked Spiral Resonator Structure

Chien-Hsun Chen, *Student Member, IEEE*, Chien-Hsiang Huang, *Student Member, IEEE*, Tzyy-Sheng Horng, *Senior Member, IEEE*, and Sung-Mao Wu, *Member, IEEE*

Abstract—This paper describes a stacked spiral resonator (SSR) structure for designing very compact multiband bandpass filters. The resonant frequencies of the proposed SSR structure can be determined by designing the spiral geometry and controlling the mutual coupling in a stacked structure. The multiple passband bandwidths can then be determined by the spacing of different layer patterns between two coupled SSRs. An adequately designed geometry of the input/output resonator with a tapped-line feed can achieve matching conditions for all passbands simultaneously. Moreover, multiple transmission zeros created on both sides of each passband provide high stopband roll-off rates.

Index Terms—Multiband bandpass filter, multilayer bandpass filter, stacked spiral resonator (SSR), transmission zeros.

I. INTRODUCTION

FOR multistandard wireless communication systems, multiband bandpass filters with a miniaturized size and high selectivity are essential components. Many efforts have been placed on developing multiband filters [1]–[18]. Implementing a dual-band bandpass filter design by combining two specific single-band filters [1]–[3] leads to a larger occupied area. An advanced concept for designing a multiband bandpass filter utilizes multimode resonators, such as stub loaded resonators (SLRs) [4]–[6], stepped-impedance resonators (SIRs) [7]–[11], and dual-mode resonators using a perturbation method [12]–[14]. A SLR configuration with a few open or short stubs can easily determine the resonant frequencies by properly adjusting the stub lengths for either a dual-band design [4], [5] or a triple-band design [6]. The two- and tri-section SIRs can easily achieve a dual-band response [7]–[9] and a triple-band response [10], [11], respectively, by designing the geometric parameters. Several dual-mode resonators of various

shape can result in dual- and triple-band bandpass filters with a pair of slits [12] or a number of open-circuited stubs [13], [14]. Although adopting multimode resonators for multiband filter designs can reduce the component size, simultaneously satisfying the design specifications of all passbands, such as the different external quality factors and coupling coefficients for each passband, is rather difficult. Other works have developed novel structures, including two sets of resonators using a combined half-wavelength SLR [15] and defected ground structure (DGS) resonator [16] or SIR [17] for implementing a multiband response. Moreover, the resonators can be assembled as a cascaded quadruplet filter with a cross coupling path to provide two transmission zeros in order to split a dual-band response into a triple-band response [18]. Although the assembled two sets of resonators can increase the degrees of freedom in extracting coupling coefficients for all passbands, the two sets of resonators require more area for implementation.

The authors' previous work [19] presented a stacked *LC* resonator with a single-mode resonant response for implementing single-band bandpass filters. Based on use of a stacked configuration, this work develops multiband bandpass filters by exploiting a stacked spiral resonator (SSR) with multimode resonant responses. The proposed SSR is embedded in a four-metal layer substrate, capable of significantly minimizing component size and providing degrees of freedom in determining coupling coefficients for each passband. Additionally, using a tapped-line feed to the input/output SSR provides a range of external quality factors for all passbands. Moreover, multiple transmission zeros are observed on both sides of individual passbands to improve the selectivity or the stopband rejection for the designed multiband bandpass filters.

II. SSRs

A. Dual-Resonance Resonator

Two-section transmission-line SIRs with half- or quarter-wavelength are frequently used for designing dual-band bandpass filters [7]–[9]. Fig. 1 depicts a two-section $\lambda/2$- and $\lambda/4$-type resonator structure, respectively, and the frequency ratios of the first two resonant modes are found as [20]

$$\left.\frac{f_2}{f_1}\right|_{\lambda/2} = \frac{\pi}{2\tan^{-1}\sqrt{R}} \tag{1}$$

$$\left.\frac{f_2}{f_1}\right|_{\lambda/4} = \frac{\pi}{\tan^{-1}\sqrt{R}} - 1 \tag{2}$$

where R denotes the impedance ratio Z_2/Z_1. The above results, as shown in Fig. 2, indicate that the second resonant frequency
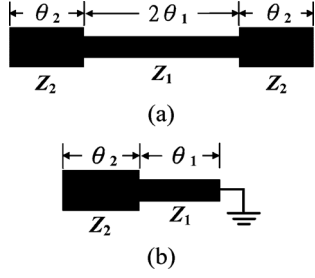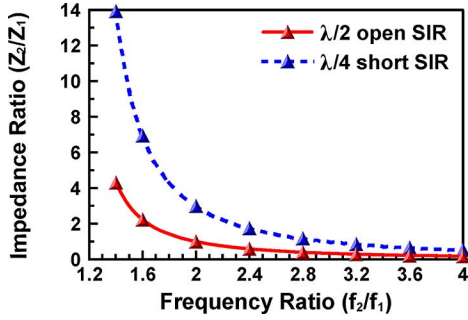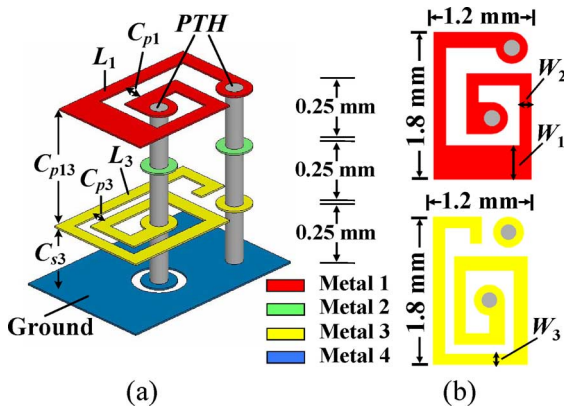
Fig. 1. Two-section SIR configurations. (a) $\lambda/2$ open (b) $\lambda/4$ short.

Fig. 2. Impedance ratio Z_2/Z_1 versus frequency ratio f_2/f_1 for the two-section $\lambda/2$ open and $\lambda/4$ short SIR.

Fig. 3. Dual-resonance SSR embedded in a four-metal layer substrate. (a) 3-D structure. (b) Metallic patterns on metal 1 and metal 3.

f_2 can be obtained by designing the impedance ratio R with a predetermined f_1. A $\lambda/4$-type resonator saves more space, but requires a larger impedance ratio than a $\lambda/2$-type one does for a specific frequency ratio. However, a high-impedance ratio design typically requires a high-impedance microstrip line that is normally restricted in the printed circuit board (PCB) process and is also considerably lossy due to high conductor loss. To overcome this problem, this work develops a dual-resonance SSR that is embedded in a four-metal layer RT/Duroid 6010 substrate with a dielectric constant of 10.2 and a loss tangent of 0.0025, as shown in Fig. 3(a). In manufacturing, there are two bonding films used to assemble three different substrates. Each bonding film between two substrates is a 0.08-mm-thick prepreg material with a dielectric constant of 4.4 and a loss tangent of
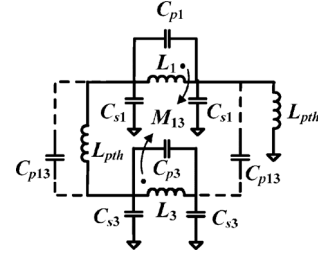

Fig. 4. Equivalent circuit of the proposed dual-resonance SSR.

0.02, which is included in the layer structure for electromagnetic (EM) simulation. It is observed that the simulated filter response shifts to slightly lower frequencies with the bonding films than without them. The microstrip sections of $Z_1(\theta_1)$ and $Z_2(\theta_2)$ in Fig. 1(b) can be represented by the spiral inductor of L_1 on metal 1 and the spiral inductor L_3 on metal 3, respectively, as shown in Fig. 3(a). The two spiral inductors shown in Fig. 3(b) are stacked vertically and connected to each other with two plated through holes (PTHs). Fig. 4 displays the equivalent circuit of the proposed dual-resonance SSR without considering the resistive loss. In Fig. 4, C_{pi} denotes the inter-coil capacitance and C_{si} represents the coil-to-ground capacitance of the spiral inductor L_i, for $i = 1$ and 3. C_{p13} and M_{13} account for the overlap capacitance and mutual inductance between L_1 and L_3, respectively. By assuming that $C_{s1} \ll C_{s3}$ and $M_{13} \ll (L_1 + 2L_{\text{PTH}})$, the first two resonant angular frequencies of the dual-resonance resonator can be derived as

$$\omega_{D1} = \sqrt{\frac{1}{2\left(C_{s3} + C_{p1}\right)L_{1T}}} \tag{3}$$

$$\omega_{D2} = \sqrt{\frac{1}{C_{s3} + C_p} \cdot \left(\frac{1}{2L_{1T}} + \frac{2}{L_3 - M_{13}}\right)} \tag{4}$$

where

$$L_{1T} = L_1 + 2L_{\text{PTH}} \tag{5}$$
$$C_p = C_{p1} + C_{p3} + C_{p13}. \tag{6}$$

The frequency ratio of ω_{D2}/ω_{D1} can be expressed as

$$\frac{\omega_{D2}}{\omega_{D1}} \approx \left(\frac{C_{s3}}{C_{s3} + C_p}\right) \cdot \left(1 + \frac{4L_{1T}}{L_3 - M_{13}}\right). \tag{7}$$

The above equation clearly indicates that the parasitic capacitance C_p and mutual inductance M_{13} significantly impact the ability to determine the frequency ratio. Notably, the spiral inductors L_1 and L_3 in Fig. 3 are wound clockwise and counterclockwise, respectively, resulting in a negative mutual inductance ($M_{13} < 0$) to decrease the frequency ratio according to (7). Therefore, in addition to more significantly reducing the component size than the conventional SIR structure, an SSR configuration provides parasitic capacitance and negative mutual inductance to reduce the frequency ratio, thus avoiding the use of a high-impedance microstrip line.
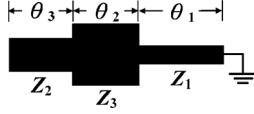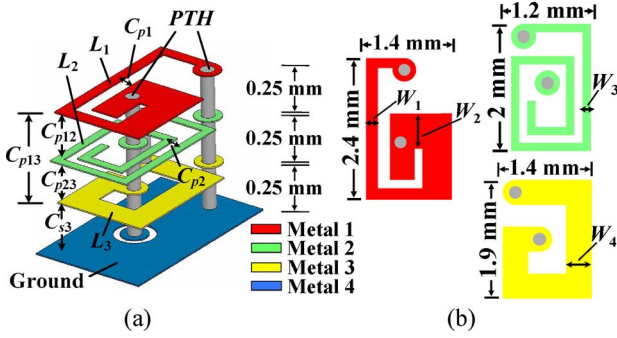
Fig. 5.   Tri-section $\lambda/4$ short SIR configuration.

Fig. 6.   Triple-resonance SSR embedded in a four-metal layer substrate. (a) 3-D structure. (b) Metallic patterns on metal 1, metal 2, and metal 3.

B. Triple-Resonance Resonator

A two-section SIR configuration can be extended to a tri-section one for triple-band bandpass filter designs [10], [11]. A previous work [21] demonstrated that the total electrical length of a $\lambda/2$-type tri-section SIR with an equal section length is shorter than a two-section one for a given operating frequency. However, the purpose of size reduction is not as obvious as in the use of a $\lambda/4$-type configuration. Fig. 5 shows a tri-section $\lambda/4$ short SIR with three microstrip sections that cause two impedance ratios $R_1 = Z_3/Z_2$ and $R_2 = Z_2/Z_1$. Additionally, the two impedance ratios can be used to determine the frequency ratios between the three resonant mode frequencies given as follows [10], [22]:

$$\frac{f_2}{f_1} = \frac{\pi}{2\tan^{-1}\sqrt{\dfrac{R_1 R_2}{1 + R_1 + R_2}}} \tag{8}$$

$$\frac{f_3}{f_1} = \frac{\pi}{\tan^{-1}\sqrt{\dfrac{R_1 R_2}{1 + R_1 + R_2}}} - 1. \tag{9}$$

Similarly, tri-section SIR structures with a lower frequency ratio require a high-impedance microstrip line that is difficult to achieve on a PCB. Similar to the concept of a dual-resonance SSR structure, a tri-section SIR can be represented by a three-layered SSR, as shown in Fig. 6, to avoid using a high-impedance microstrip line. The microstrip sections of $Z_1(\theta_1)$, $Z_2(\theta_2)$, and $Z_3(\theta_3)$ in Fig. 5 are represented by the spiral inductors L_1, L_2, and L_3 on metal 1, metal 2, and metal 3, respectively. The three spiral inductors are connected as a triple-resonance SSR by using two PTHs. Fig. 7 illustrates the equivalent circuit of the proposed triple-resonance SSR without considering the resistive loss. In Fig. 7, C_{pi} and C_{si} are the parasitic inter-coil capacitance and coil-to-ground capacitance, respectively. Moreover, C_{pij} and M_{ij} represent the overlap capacitance and the mutual inductance, respectively, between the adjacent spiral inductors L_i and L_j. By assuming that C_{p3},
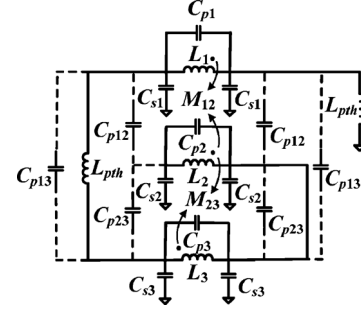

Fig. 7.   Equivalent circuit of the proposed triple-resonance SSR.

$C_{p13}, C_{s1} \ll C_{s3}, M_{12} \ll (L_1 + 2L_{\text{PTH}})$, and $M_{23} \ll L_2$, the first three resonant frequencies of the proposed triple-resonance SSR can be obtained as

$$\omega_{T1} = \sqrt{\frac{1}{2\left(C_{s3} + C_{p1}\right) L_{1T}}} \tag{10}$$

$$\omega_{T2} = \sqrt{\frac{1}{2\left(L_2 - M_{12}\right)} \cdot \left(\frac{1}{C_{s3}} + \frac{1}{C_p - 2C_{p2}}\right)} \tag{11}$$

$$\omega_{T3} = \sqrt{\frac{1}{2L_{1T}C_{s3}} + \frac{1}{C_{s3}\left(L_3 - M_{23}\right)} + \frac{2}{C_p\left(L_2 - M_{12}\right)}} \tag{12}$$

where

$$L_{1T} = L_1 + 2L_{\text{PTH}} \tag{13}$$
$$C_p = C_{p1} + C_{p2} + C_{p12} + C_{p23}. \tag{14}$$

The first resonant frequency ω_{T1} depends on L_1, L_{PTH}, C_{p1}, and C_{s3}. After ω_{T1} is known from specifying the values of these three elements, the second resonant frequency ω_{T2} can be subsequently determined by L_2. The spiral inductance L_3 then determines the third resonant frequency ω_{T3} with knowledge of ω_{T1} and ω_{T2}. Finally, the frequency ratios of ω_{T2}/ω_{T1} and ω_{T3}/ω_{T1} for the proposed triple-resonance SSR can be represented as

$$\frac{\omega_{T2}}{\omega_{T1}} = \left(1 + \frac{C_{s3}}{C_p - 2C_{p2}}\right) \cdot \left(\frac{L_{1T}}{L_2 - M_{12}}\right) \tag{15}$$

$$\frac{\omega_{T3}}{\omega_{T1}} = \left(1 + \frac{2L_{1T}}{L_3 - M_{23}}\right) + \left(\frac{C_{s3} - C_p}{C_p}\right) \cdot \left(\frac{4L_{1T}}{L_2 - M_{12}}\right) \cdot \tag{16}$$

Notably, the parasitic capacitance C_p and the mutual inductance M_{12} and M_{23} of the stacked resonator substantially influence the two frequency ratios. Similar to the above mentioned treatment, the spiral inductors L_1 and L_3 were wound clockwise, while the spiral inductor L_2 was wound counterclockwise. In doing so, the negative mutual inductances ($M_{12} < 0$ and $M_{23} < 0$) were obtained to reduce the two frequency ratios without adjusting the geometry of spiral inductors.

III. DUAL-BAND BANDPASS FILTER DESIGN

To demonstrate the feasibility of the proposed design concept, this work designs a second-order 0.2-dB equal-ripple Cheby-
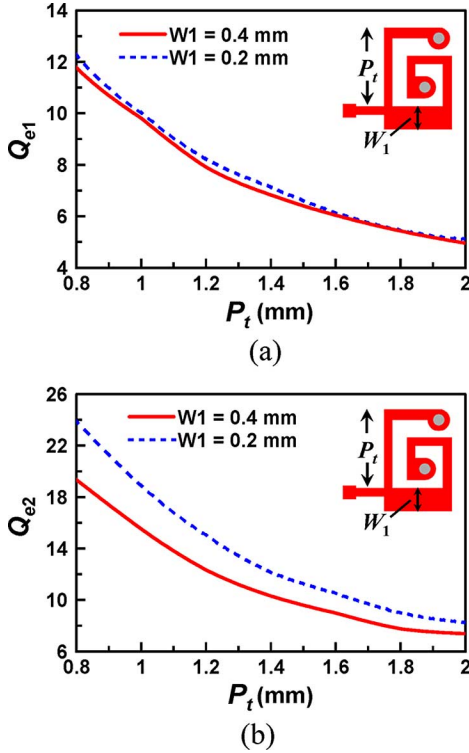
Fig. 8. External quality factors versus the tapped feed position for the dual-resonance SSR. (a) Band 1. (b) Band 2.
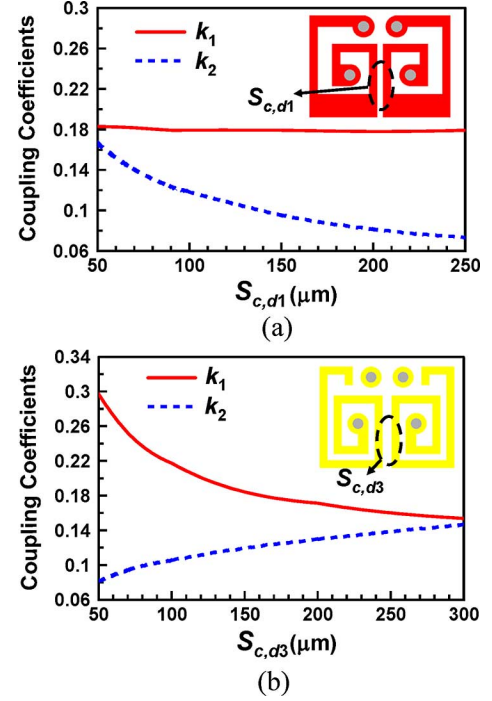

Fig. 9. Coupling coefficients versus the coupling spacing on different metal layers for the coupled dual-resonance SSRs. (a) Metal 1 (b) Metal 3.

shev dual-band bandpass filter with the passband center frequencies at $f_1 = 2.45$ GHz and $f_2 = 5.2$ GHz. This design is achieved by using the dual-resonance SSR shown in Fig. 3 for wireless local area network (WLAN) applications. The adopted filter prototype element values are $g_1 = 1.038$, $g_2 = 0.675$, and $g_3 = 1.539$. The fractional bandwidths of the first and second passbands are set as $\Delta_1 = 15\%$ and $\Delta_2 = 10\%$, respectively. The external quality factor Q_{ei} and coupling coefficient k_i can be found in terms of the filter prototype elements as

$$k_i = \frac{\Delta_i}{\sqrt{g_1 g_2}} \qquad (17)$$

$$Q_{ei} = \frac{g_0 g_1}{\Delta_i} = \frac{g_2 g_3}{\Delta_i}. \qquad (18)$$

The above design parameters are evaluated as $Q_{e1} = 6.9$ and $k_1 = 0.18$ for the first passband and $Q_{e2} = 10.4$ and $k_2 = 0.12$ for the second passband. To obtain the physical dimension of the proposed dual-band bandpass filter, the external quality factors and coupling coefficients are related to the tapped position P_t and the coupling spacing on different metal layers $S_{c,di}$, for $i = 1$ and 3, respectively [23], with the assistance of EM simulation by Ansys-Ansoft HFSS. Fig. 8(a) and (b) illustrates the external quality factors Q_{e1} and Q_{e2}, respectively, with respect to the tapped position of P_t for different values of the specified width W_1 on metal 1. According to these figures, varying W_1 obviously changes Q_{e2}, yet only a slight change in Q_{e1} for the same tapped feed position. Therefore, Q_{e1} and Q_{e2} can be individually determined by controlling P_t and W_1, respectively.

Notably, slightly tuning the width W_1 makes the resonant frequencies almost unchanged. If a tuning of W_1 significantly

changes the designed resonant frequencies, compensation can be made by simply varying the length or inductance of spiral patterns on different metal layers. It is also noted that $Q_{e2} > Q_{e1}$ for the results shown in Fig. 8. To conversely achieve $Q_{e2} < Q_{e1}$, increasing the spiral turn spacing on metal 3 provides the most effectiveness for a given spiral inductance L_3.

Fig. 9(a) and (b) displays the coupling coefficients with respect to the spacing $S_{c,d1}$ on metal 1 and the spacing $S_{c,d3}$ on metal 3, respectively. According to Fig. 9(a), an increase in $S_{c,d1}$ decreases the coupling coefficient of the second passband k_2 without altering the coupling coefficient of the first passband k_1. The reason behind it is as follows. In this design, electric coupling dominates the coupling of the SSRs. It has been further found from HFSS simulation that the electric coupling between two metal-1 spiral patterns is weak at the frequencies of band 1, but gets much stronger at the frequencies of band 2, which provides evidence for the dependence of k_1 and k_2 on the spacing of $S_{c,d1}$, as shown in Fig. 9(a). Consequently, k_1 and k_2 can also be individually determined by controlling $S_{c,d1}$ and $S_{c,d3}$, respectively. A detailed design procedure is summarized in the following steps.

Step 1) Choose the tapped feed position that is located at $P_t = 1.4$ mm with $W_1 = 0.4$ mm, as shown in Fig. 8, to fulfill the design requirements of $Q_{e1} = 6.9$ and $Q_{e2} = 10.4$;

Step 2) Fig. 9(b) shows the relation of k_1 and k_2 versus the spacing $S_{c,d3}$ on metal 3 when $S_{c,d1}$ is equal to 0.1 mm. Also select $S_{c,d3} = 0.17$ mm to obtain the coupling coefficient $k_1 = 0.18$ for the first passband.

Step 3) Fig. 9(a) shows the relation of k_1 and k_2 versus the spacing $S_{c,d1}$ when $S_{c,d3}$ equals 0.17 mm since the
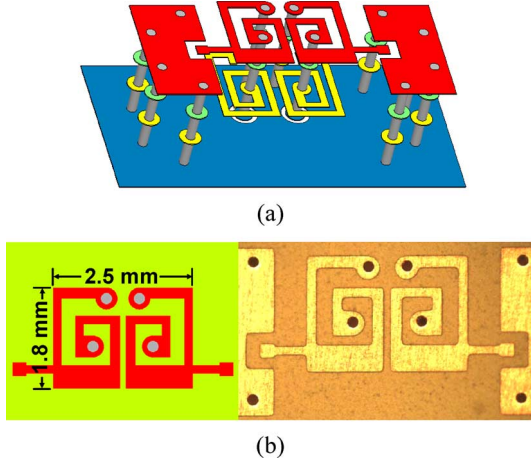
Fig. 10. Proposed dual-band bandpass filter design using two coupled dual-resonance SSRs. (a) 3-D geometrical configuration. (b) Top view layout and photograph.
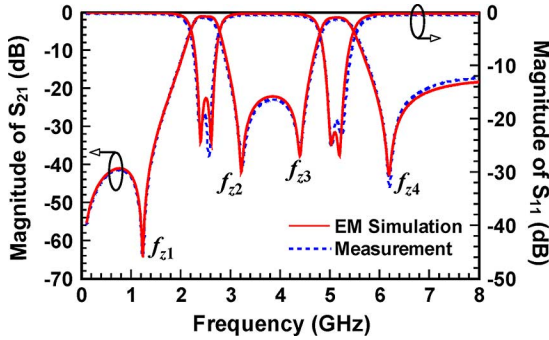

Fig. 11. Comparison of the magnitude of S_{21} and S_{11} between EM simulation and measurement for the proposed dual-band bandpass filter design.

change of $S_{c,d1}$ only slightly impacts k_1. Also, select $S_{c,d1} = 0.1$ mm to obtain $k_2 = 0.12$ and preserve $k_1 = 0.18$.

Fig. 10 shows the 3-D geometrical configuration, top view layout, and photograph of the designed second-order dual-band bandpass filter. The occupied area, excluding the tapped line, is 2.5 mm $\times$ 1.8 mm, revealing an ultra-compact component size compared with conventional microstrip dual-band filters.

Fig. 11 compares the magnitudes of S_{21} and S_{11} between HFSS simulation and measurement, indicating a good agreement over a frequency range up to 8 GHz. The measured return losses in the two passbands exceed 19 dB. The insertion losses are less than 1.2 and 1.7 dB in the first and second passband, respectively. The four transmission zeros located at 1.2, 3.2, 4.4, and 6.2 GHz enhance the rolloff rates on both sides of the two passbands. These transmission zeros come from coexistence of electric and magnetic coupling [24] and depend on the spacing $S_{c,d1}$ and $S_{c,d3}$. For this case, $S_{c,d1}$ and $S_{c,d3}$ are given as 0.1 and 0.18 mm, respectively. The four transmission-zero frequencies denoted as f_{zi}, for $i = 1, 2, 3$, and 4, are discussed in detail as follows.

A change in the spacing $S_{c,d1}$ or the spacing $S_{c,d3}$ causes a frequency shift Δf_{zi} in the transmission-zero frequency f_{zi}. As $\Delta f_{zi} > 0$, the transmission-zero frequency f_{zi} moves toward a higher frequency. In contrast, as $\Delta f_{zi} < 0$, the
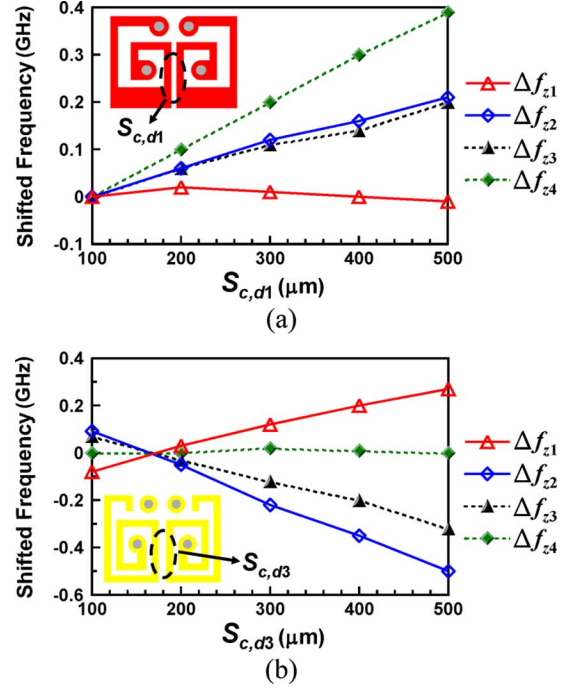

Fig. 12. Transmission-zero frequencies versus the coupling spacing on different metal layers for the proposed dual-band bandpass filter design. (a) Metal 1. (b) Metal 3.

transmission-zero frequency f_{zi} shifts to a lower frequency. Fig. 12(a) and (b) illustrates the frequency shift Δf_{zi} with respect to the spacing $S_{c,d1}$ and the spacing $S_{c,d3}$, respectively. According to Fig. 12(a), increasing $S_{c,d1}$ on metal 1 pushes f_{z2}, f_{z3}, and f_{z4} toward higher frequencies and retains f_{z1} at 1.2 GHz. Fig. 12(b) also reveals that an increase in $S_{c,d3}$ causes f_{z1} and f_{z2} to shift close to the first passband, f_{z3} to move far away the second passband, and f_{z4} to remain at 6.2 GHz. Notably, the spacings $S_{c,d1}$ and $S_{c,d3}$ influence both the transmission-zero frequencies and the design conditions of the coupling coefficient for the two passbands. Therefore, passband performance and transmission zeros should be taken into account simultaneously in the design procedure.

IV. TRIPLE-BAND BANDPASS FILTER DESIGN

The SSR structure can also be used to construct a triple-resonance resonator in order to realize a triple-band bandpass filter. As an example, a second-order 0.2-dB equal-ripple Chebyshev triple-band bandpass filter is designed with the passband center frequencies at $f_1 = 2.1$ GHz, $f_2 = 3.5$ GHz, and $f_3 = 5.8$ GHz for WCDMA/WiMAX/WLAN applications using the triple-resonance SSR in Fig. 6. The fractional bandwidths for the triple-band response are designed as $\Delta_1 = 15\%$, $\Delta_2 = 12\%$, and $\Delta_3 = 9\%$, respectively. The estimated external quality factors and coupling coefficients are also obtained as $Q_{e1} = 6.9$ and $k_1 = 0.18$ for the first passband, $Q_{e2} = 8.6$ and $k_2 = 0.14$ for the second passband, and $Q_{e3} = 11.5$ and $k_3 = 0.11$ for the third passband. The external quality factors and coupling coefficients of each passband can be evaluated as a function of the tapped position P_t and the coupling spacing on different metal layers $S_{c,ti}$, for $i = 1, 2$, and 3 with the help of HFSS simulation. Fig. 13(a)–(c) displays the design curves of Q_{e1}, Q_{e2}, and
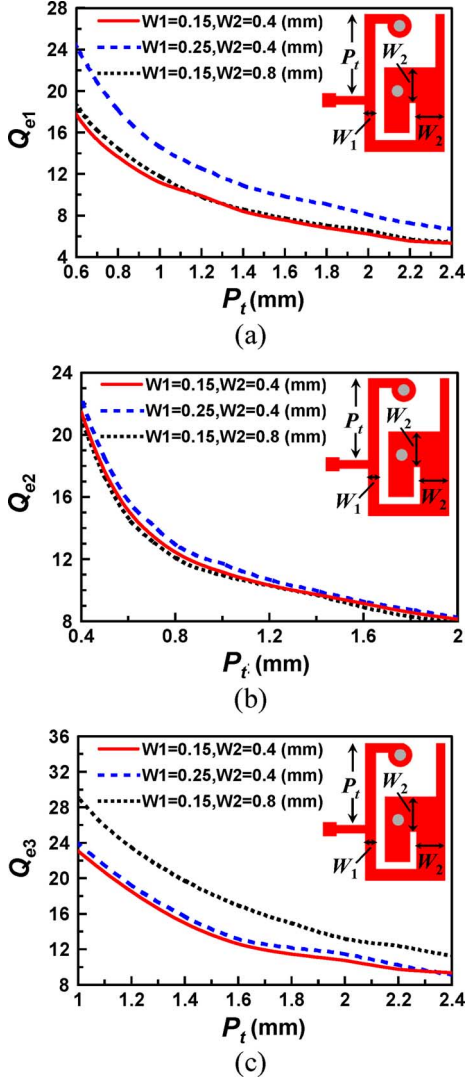
Fig. 13. External quality factors versus the tapped feed position for the triple-resonance SSR. (a) Band 1. (b) Band 2. (c) Band3.
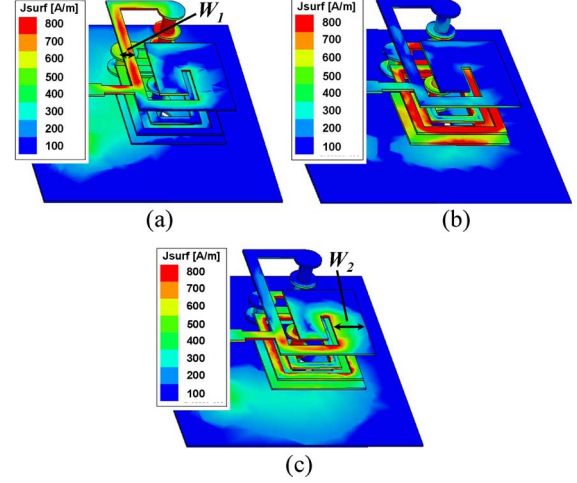

Fig. 14. Simulated current distribution on the triple-resonance SSR. (a) At the first resonant frequency. (b) At the second resonant frequency. (c) At the third resonant frequency.

Q_{e3}, respectively, with respect to P_t for different combination of the specified widths W_1 and W_2 on metal 1. According to Fig. 13(a) and (c), an increase in W_1 increases the value of Q_{e1}, yet hardly changes the value of Q_{e3}. Conversely, an increase in W_2 enlarges the value of Q_{e3}, yet barely affects the value of Q_{e1}. Moreover, the change of W_1 or W_2 negligibly influences Q_{e2}, as shown in Fig. 13(b). Therefore, Q_{e2} can be made smaller or larger than Q_{e1} and Q_{e3} by increasing or decreasing both W_1 and W_2.

To further explain Fig. 13 with an EM point of view, Fig. 14 shows the simulated current distribution on the triple-resonance SSR at the three main resonant frequencies. As shown in Fig. 14(a) and (c), the current distribution concentrates on the different portion of the metal-1 spiral pattern with different width of W_1 and W_2 at the first and third resonant frequency, respectively. It is therefore reasonable to observe that increasing W_1 enlarges Q_{e1} rather than Q_{e3}, whereas increasing W_2 has the converse effect. Moreover, it can be seen from Fig. 14(b) that the currents mainly concentrate on metal 2 and 3 and weaken on metal 1 at the second resonant frequency.

This can explain why the change of the width W_1 and W_2 on the metal-1 spiral pattern hardly influences Q_{e3}.

As a matter of fact, all of the external quality factors for a triple-band response can be individually determined by the following procedure: First, determine the tapped feed position P_t at the input/output resonator based on the calculated value of Q_{e2}; Second, determine the width W_1 from the design value of Q_{e1}; Finally, determine the width W_2 from the estimated value of Q_{e3}. The next step determines the spacing in each layer to obtain the calculated coupling coefficients for each passband. Fig. 15(a)–(c) shows the design curves of the coupling coefficients with respect to the spacing of $S_{c,t1}$ on metal 1, the spacing $S_{c,t2}$ on metal 2, and the spacing $S_{c,t3}$ on metal 3, respectively. As mentioned earlier in the dual-band BPF design, the coupling coefficients k_1, k_2, and k_3 corresponding to the first, second, and third passband, respectively, can also be individually determined by adequately controlling the spacings $S_{c,t1}$, $S_{c,t2}$, and $S_{c,t3}$. Moreover, an extra metallic stub on the right edge of the SSR on metal 1, as shown in Fig. 13, can be used to enhance these coupling coefficients. The design procedure for the proposed triple-band bandpass filter is summarized as follows.

1) Under the condition of $W_1 = 0.15$ mm and $W_2 = 0.4$ mm in Fig. 13, choose the tapped feed position at $P_t = 1.8$ mm to correspond to the external quality factors $Q_{e1} = 6.9$, $Q_{e2} = 8.6$, and $Q_{e3} = 11.5$ for achieving the design requirement.

2) Fig. 15(c) shows the coupling coefficients versus the spacing $S_{c,t3}$ on metal 3, while $S_{c,t1} = 0.1$ mm and $S_{c,t2} = 0.5$ mm. Also, choose $S_{c,t3} = 0.14$ mm to obtain the coupling coefficient $k_1 = 0.18$ for the first passband.

3) Fig. 15(a) shows the coupling coefficients versus the spacing $S_{c,t1}$ on metal 1, while $S_{c,t2} = 0.5$ mm and $S_{c,t3} = 0.14$ mm since k_1 reveals a weak dependence on $S_{c,t1}$. Also, choose $S_{c,t1} = 0.1$ mm to provide $k_3 = 0.11$ for the third passband and preserve $k_1 = 0.18$.

4) Fig. 15(b) shows the coupling coefficients versus the spacing $S_{c,t2}$ on metal 2 since k_1 and k_3 vary slightly
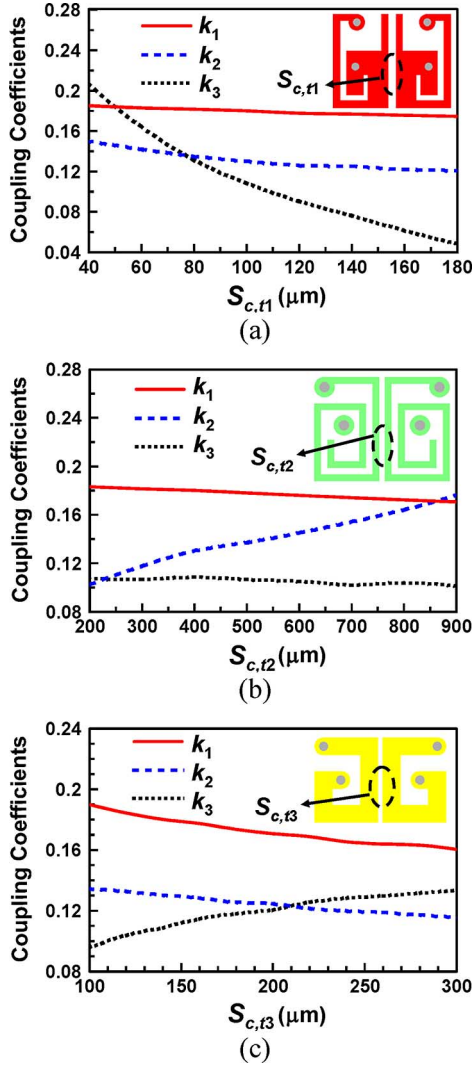
Fig. 15. Coupling coefficients versus the coupling spacing on different metal layers for the coupled triple-resonance SSRs. (a) Metal 1. (b) Metal 2. (c) Metal 3.
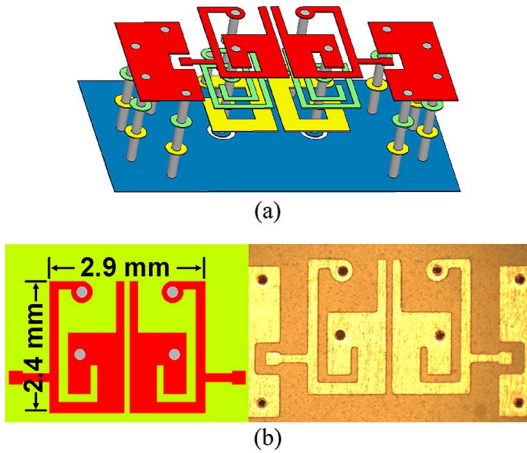

Fig. 16. Proposed triple-band bandpass filter design using two coupled triple-resonance SSRs. (a) 3-D geometrical configuration. (b) Top view layout and photograph.

over a range of $S_{c,t2}$ from 0.3 to 1 mm. Also, choose $S_{c,t2} = 0.7$ mm to obtain $k_2 = 0.14$ and retain $k_1 = 0.18$ and $k_3 = 0.11$ simultaneously.
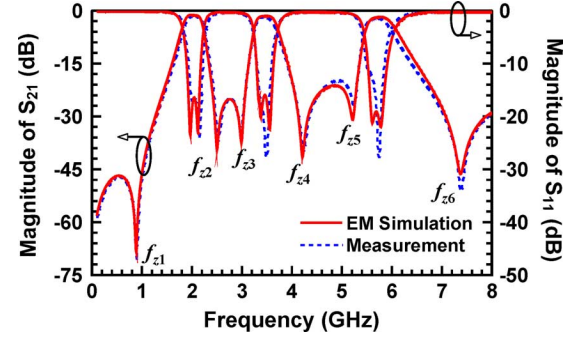

Fig. 17. Comparison of the magnitude of S_{21} and S_{11} between EM simulation and measurement for the proposed triple-band bandpass filter design.

Fig. 18. Transmission-zero frequencies versus the coupling spacing on different metal layers for the proposed triple-band bandpass filter design. (a) Metal 1. (b) Metal 2. (c) Metal 3.

Fig. 16 illustrates the 3-D geometrical configuration, top view layout, and photograph of the designed second-order triple-band bandpass filter. The occupied area, excluding the tapped line, is 2.9 mm × 2.4 mm.

Fig. 17 compares the magnitudes of S_{21} and S_{11} between HFSS simulation and measurement for the proposed triple-band bandpass filter design, indicating a good agreement over a frequency range up to 8 GHz. The measured insertion losses are lower than 1.4, 1.7, and 2 dB in the first, second, and third passband, respectively, while the measured return losses are all exceed 15 dB. According to Fig. 17, each passband has a pair of

transmission zeros on both sides. They are due to coexistence of magnetic and electric coupling and located at 0.9 and 2.4 GHz with respect to the first passband, at 3 and 4.2 GHz with respect to the second passband, and at 5.2 and 7.2 GHz with respect to the third passband.

Similarly, varying the spacing $S_{c,t1}$, $S_{c,t2}$, and $S_{c,t3}$ causes a frequency shift Δf_{zi} in the transmission-zero frequency f_{zi}. The transmission-zero frequency f_{zi} also shifts to the higher and lower frequency for $\Delta f_{zi} > 0$ and $\Delta f_{zi} < 0$, respectively. Fig. 18 illustrates the frequency shift Δf_{zi} versus the spacing $S_{c,t1}$, $S_{c,t2}$, and $S_{c,t3}$. According to Fig. 18(a), increasing $S_{c,t1}$ moves the transmission-zero frequencies f_{z5} and f_{z6} close to the third passband without altering the other transmission-zero frequencies. Fig. 18(b) reveals that an increase in $S_{c,t2}$ shifts the two transmission-zero frequencies f_{z2} and f_{z3} to lower frequencies, while the other ones only exhibit a slight change. According to Fig. 18(c), an increase in $S_{c,t3}$ shifts the transmission-zero frequencies f_{z1} and f_{z2} that are on both sides of the first passband to higher frequencies. Meanwhile, the transmission-zero frequencies f_{z3} and f_{z4} near the second passband are nearly unchanged, and the transmission-zero frequencies f_{z5} and f_{z6} near the third passband are shifted toward lower frequencies. Notably, although adjusting $S_{c,t1}$, $S_{c,t2}$, or $S_{c,t3}$ can flexibly move the transmission-zero frequencies, special care is necessary to deal with the effects on coupling coefficients.

V. CONCLUSION

This paper has described very compact dual- and triple-band bandpass filters based on SSRs. The resonant frequencies of the proposed SSRs depend on both the geometry of spiral patterns in different metal layers and the spacing between the adjacent spiral patterns in the same layer. The tapped-feed structure applied to the proposed SSR with a spiral pattern of nonuniform width on metal 1 can flexibly provide an appropriate external quality factor to achieve the impedance matching condition. Additionally, controlling the spacing between two spiral patterns in different metal layers offer superior degrees of freedom to individually determine the bandwidth of each passband for a multiband bandpass filter design. Moreover, multiple transmission zeros are created on both sides of each passband to significantly improve the roll-off rate and attenuation in the stopband.

REFERENCES

[1] X. Y. Zhang and Q. Xue, "Novel dual-mode dual-band filters using coplanar-waveguide-fed ring resonators," *IEEE Trans. Microw. Theory Tech.*, vol. 55, no. 10, pp. 2183–2190, Oct. 2007.

[2] E. E. Djoumessi and K. Wu, "Multilayer dual-mode dual-bandpass filter," *IEEE Microw. Wireless Compon. Lett.*, vol. 19, no. 1, pp. 21–23, Jan. 2009.

[3] X. Luo, H. Qian, J.-G. Ma, K. Ma, and K. S. Yeo, "Compact dual-band bandpass filters using novel embedded spiral resonator (ESR)," *IEEE Microw. Wireless Compon. Lett.*, vol. 20, no. 8, pp. 435–437, Aug. 2010.

[4] P. Mondal and M. K. Mandal, "Design of dual-band bandpass filters using stub-loaded open-loop resonators," *IEEE Trans. Microw. Theory Tech.*, vol. 56, no. 1, pp. 150–155, Jan. 2008.

[5] Z. Zhang, Y.-C. Jiao, X.-M. Wang, and S.-F. Cao, "Design of a compact dual-band bandpass filter using opposite hook-shaped resonator," *IEEE Microw. Wireless Compon. Lett.*, vol. 21, no. 7, pp. 359–361, Jul. 2011.

[6] Q.-X. Chu, F.-C. Chen, Z.-H. Tu, and H. Wang, "A novel crossed resonator and its applications to bandpass filters," *IEEE Trans. Microw. Theory Tech.*, vol. 57, no. 7, pp. 1753–1759, Jul. 2009.

[7] P. K. Singh, S. Basu, and Y.-H. Wang, "Miniature dual-band filter using quarter wavelength stepped impedance resonators," *IEEE Microw. Wireless Compon. Lett.*, vol. 18, no. 2, pp. 88–90, Feb. 2008.

[8] Y.-C. Chang, C.-H. Kao, M.-H. Weng, and R.-Y. Yang, "Design of the compact dual-band bandpass filter with high isolation for GPS/WLAN applications," *IEEE Microw. Wireless Compon. Lett.*, vol. 19, no. 12, pp. 780–782, Dec. 2009.

[9] C.-H. Tseng and H.-Y. Shao, "A new dual-band microstrip bandpass filter using net-type resonators," *IEEE Microw. Wireless Compon. Lett.*, vol. 20, no. 4, pp. 196–198, Apr. 2010.

[10] C.-I. G. Hsu, C.-H. Lee, and Y.-H. Hsieh, "Tri-band bandpass filter with sharp passband skirts designed using tri-section SIRs," *IEEE Microw. Wireless Compon. Lett.*, vol. 18, no. 1, pp. 19–21, Jan. 2008.

[11] Q.-X. Chu and X.-M. Lin, "Advanced triple-band bandpass filter using tri-section SIR," *Electron. Lett.*, vol. 44, no. 4, pp. 295–296, Feb. 2008.

[12] Y. Sung, "Dual-mode dual-band filter with band notch structures," *IEEE Microw. Wireless Compon. Lett.*, vol. 20, no. 2, pp. 73–75, Feb. 2010.

[13] S. Luo, L. Zhu, and S. Sun, "A dual-band ring-resonator bandpass filter based on two pairs of degenerate modes," *IEEE Trans. Microw. Theory Tech.*, vol. 58, no. 12, pp. 3427–3432, Dec. 2010.

[14] S. Luo, L. Zhu, and S. Sun, "Compact dual-mode triple-band bandpass filters using three pairs of degenerate modes in a ring resonator," *IEEE Trans. Microw. Theory Tech.*, vol. 59, no. 5, pp. 1222–1229, May 2011.

[15] X. Y. Zhang, Q. Xue, and B. J. Hu, "Planar tri-band bandpass filter with compact size," *IEEE Microw. Wireless Compon. Lett.*, vol. 20, no. 5, pp. 262–264, May 2010.

[16] X. Lai, C.-H. Liang, H. Di, and B. Wu, "Design of tri-band filter based on stub loaded resonator and DGS resonator," *IEEE Microw. Wireless Compon. Lett.*, vol. 20, no. 5, pp. 265–267, May 2010.

[17] M. Zhou, X. Tang, and F. Xiao, "Compact dual band transversal bandpass filter with multiple transmission zeros and controllable bandwidths," *IEEE Microw. Wireless Compon. Lett.*, vol. 19, no. 6, pp. 347–349, Jun. 2009.

[18] B.-J. Chen, T.-M. Shen, and R.-B. Wu, "Design of tri-band filters with improved band allocation," *IEEE Trans. Microw. Theory Tech.*, vol. 57, no. 7, pp. 1790–1797, Jul. 2009.

[19] C.-H. Chen, C.-H. Huang, T.-S. Horng, S.-M. Wu, J.-Y. Li, C.-C. Chen, C.-T. Chiu, and C.-P. Hung, "Very compact stacked *LC* resonator-based bandpass filters with a novel approach to tune the transmission zeros," *IEEE Microw. Wireless Compon. Lett.*, vol. 19, no. 5, pp. 293–295, May 2009.

[20] M. Sagawa, M. Makimoto, and S. Yamashita, "Geometrical structures and fundamental characteristics of microwave stepped-impedance resonators," *IEEE Trans. Microw. Theory Tech.*, vol. 45, no. 7, pp. 1078–1085, Jul. 1997.

[21] D. Packiaraj, M. Ramesh, and A.-T. Kalghatgi, "Design of a tri-section folded SIR filter," *IEEE Microw. Wireless Compon. Lett.*, vol. 16, no. 5, pp. 317–319, May 2006.

[22] C.-H. Lee, C.-I. G. Hsu, and L.-Y. Chen, "Band-notched ultra-wide-band bandpass filter design using combined modified quarter-wavelength tri-section stepped-impedance resonator," *IET Microw. Antennas Propag.*, vol. 3, no. 8, pp. 1232–1236, Dec. 2009.

[23] J.-S. Hong and M. J. Lancaster, *Microstrip Filters for RF/Microwave Applications*. New York: Wiley, 2001, pp. 109–272.

[24] Q.-X. Chu and H. Wang, "A compact open-loop filter with mixed electric and magnetic coupling," *IEEE Trans. Microw. Theory Tech.*, vol. 56, no. 2, pp. 431–439, Feb. 2008.

Chien-Hsun Chen (S'08) was born January 30, 1981, in Kaohsiung, Taiwan. He received the B.S.E.E degree from the Yuan-Ze University, Taoyuan, Taiwan, in 2003, the M.S.E.E. degree from I-Shou University, Kaohsiung, Taiwan, in 2005, and is currently working toward the Ph.D. degree in electrical engineering at National Sun Yet-Sen University, Kaohsiung, Taiwan.

His research interests are the design and analysis of embedded and integrated passive components for wireless communications.

Chien-Hsiang Huang (S'08) was born August 24, 1978, in Kaohsiung, Taiwan. He received the B.S.E.E., M.S.E.E., and Ph D. degrees from National Sun Yat-Sen University, Kaohsiung, Taiwan, in 2000, 2002, and 2011, respectively.

He is currently a Research and Development Engineer with the Realtek Semiconductor Corporation, HsinChu, Taiwan. His main research interests are design and modeling of RF/microwave integrated passive devices.

Dr. Horng has served on several Technical Program Committees of international conferences including the International Association of Science and Technology for Development (IASTED), International Conference on Wireless and Optical Communications, the IEEE Region 10 International Technical Conference, the IEEE International Workshop on Electrical Design of Advanced Packaging and Systems, the Asia–Pacific Microwave Conference, the IEEE Radio and Wireless Symposium, and the Electronic Components and Technology Conference. He was the recipient of the 1996 Young Scientist Award presented by the International Union of Radio Science, the 1998 Industry–Education Cooperation Award presented by the Ministry of Education, Taiwan, and the 2010 Distinguished Electrical Engineer Award presented by the Chinese Institute of Electrical Engineering, Taiwan.

Tzyy-Sheng Horng (S'88–M'92–SM'05) was born in Taichung, Taiwan, on December 7, 1963. He received the B.S.E.E. degree from National Taiwan University, Taipei, Taiwan, in 1985, and the M.S.E.E. and Ph.D. degrees from the University of California at Los Angeles (UCLA), in 1990 and 1992, respectively.

Since August 1992, he has been with the Department of Electrical Engineering, National Sun Yat-Sen University, Kaohsiung, Taiwan, where he was the Director of the Telecommunication Research and Development Center (2003–2008) and Director of the Institute of Communications Engineering (2004–2007), and where he is currently a Professor and the Advanced Semiconductor Engineering Inc. (ASE Inc.) Chair Professor. He has authored or coauthored over 100 technical publications published in IEEE journals and conferences proceedings. He holds over ten patents. His research interests include RF and microwave integrated circuits and components, RF signal integrity for wireless system-in-package, digitally assisted RF technologies, and green radios for cognitive sensors and Doppler radars.

Sung-Mao Wu (M'96) was born in Kaohsiung, Taiwan, on January 29, 1971. He received the M.S.E.E. degree from the Yulin University of Science and Technology, Yulin, Taiwan, in 1996, and the Ph.D. degree from National Sun Yet-Sen University, Kaohsiung, Taiwan, in 2001.

From July 2000 to March 2006, he was with the Research and Development Electrical Laboratory, Advance Semiconductor Engineering (ASE), in charge of system-in-package (SiP) circuit design and analysis. Since April 2006, he has been with the Department of Electrical Engineering, National University of Kaohsiung, Kaohsiung, Taiwan, initially as an Assistant Professor, and currently as an associate Professor. His research fields are in the 3-D SiP (3-D-SiP) and RF integrated circuit (RFIC) design and testing technologies.